

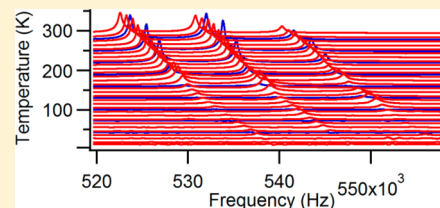
Ca-Doping of BiFeO₃: The Role of Strain in Determining Coupling between Ferroelectric Displacements, Magnetic Moments, Octahedral Tilting, and Oxygen-Vacancy Ordering

Jason A. Schiemer,^{*,†} Ray L. Withers,[‡] Yun Liu,[‡] and Michael A. Carpenter[†]

[†]Department of Earth Sciences, University of Cambridge, Downing Street, Cambridge CB2 3EQ, United Kingdom

[‡]Research School of Chemistry, Australian National University, Science Road, Canberra, ACT 0200, Australia

ABSTRACT: Elastic and anelastic properties of a member of the BiFeO₃–CaFeO_{2.5} perovskite solid solution (BCFO), which is known to have multiple instabilities, have been investigated by resonant ultrasound spectroscopy. This phase, with 64% Bi and 36% Ca on the A site, is antiferromagnetic ($T_N \sim 650$ K) and has an ordered arrangement of oxygen vacancies with tetragonal lattice geometry. The inverse mechanical quality factor, Q^{-1} , has a maximum near 100 K, correlating closely with a peak in dielectric loss, reported previously, consistent with a loss mechanism that involves the movement of oxygen vacancies accompanied by local lattice distortion. At higher temperature, there is a further acoustic loss peak that is correlated with complex impedance anomalies. There is no clear relationship to the magnetic transition, and the observations are interpreted as relating to ionic conductivity. A small stiffening, scaling with the square of the magnetic order parameter below T_N , indicates that the main coupling with strain is biquadratic, confirming that conventional coupling of magnetic order with symmetry-breaking shear strains is weak in BCFO. Data from the literature for BCFO indicates that local strain fields are likely to be responsible for suppressing the spin cycloid present in BiFeO₃.



KEYWORDS: strain, elasticity, resonant ultrasound spectroscopy, incommensurate, relaxation, multiferroic

INTRODUCTION

BiFeO₃ (BFO) has been the focus of intense interest for its particular multiferroic (ferroelectric, ferroelastic, and antiferromagnetic) properties.^{1–3} Aside from the difficulties in making pure, stoichiometric samples, however, a key issue has been that the cycloidal arrangement of individual moments in the antiferromagnetic structure precludes the development of a remnant magnetic moment under ambient conditions. An additional goal, therefore, has been to identify dopants that might assist with the issues of stability and synthesis, lead to a canting geometry that gives ferromagnetism, provide a means of controlling the nature and strength of magnetoelectric coupling, and generate mechanisms for engineering transformation-related microstructures. Doping with Ca (BCFO) has proved to be promising in this context, primarily because the cycloidal magnetic structure is replaced by a canted antiferromagnetic structure that is indeed weakly ferromagnetic.^{4–10} High levels of doping go beyond simply modifying the properties of the end member phase, however, and lead to additional properties relating particularly to the presence of oxygen vacancies. In the present study, the primary objective was to investigate the role of strain in determining coupling phenomena through observations of elastic and anelastic relaxations related to magnetic ordering, oxygen-vacancy dynamics, and ionic conductivity when the doping is at a relatively high level (36% Bi replaced by Ca). These provide particular insights into the influence of both local and

macroscopic strain and provide an informative contrast to behavior at low dopant levels.

Desirable (or undesirable) changes in multiferroic properties are directly related to changes in structure. Influences of chemistry on the latter are most simply reflected in the topology of a subsolidus phase diagram. Charge compensation for the substitution of Ca^{II} for Bi^{III} in BCFO could occur by the introduction of vacancies on oxygen sites or by oxidation of Fe^{III} to Fe^{IV}, giving theoretical solid solutions between BiFeO₃ and CaFe^{III}O_{2.5} or CaFe^{IV}O₃, respectively. CaFeO₃ can be produced under special conditions of high oxygen pressure and has the *Pnma* structure (R- and M-point octahedral tilting; unit cell $2a_p^{1/2} \times 2a_p \times 2a_p^{1/2}$, where a_p is the edge dimension of the primitive parent structure) at room temperature.^{11–14} It has interesting properties in its own right, including a charge disproportion transition (*Pnma* → *P2₁/n*, $2\text{Fe}^{\text{IV}} \rightarrow \text{Fe}^{\text{III}} + \text{Fe}^{\text{V}}$) below ~ 290 K^{12,14} and magnetic ordering to an incommensurate antiferromagnetic structure^{14,15} below a Néel temperature, T_N , of 115¹¹ or 127 K.¹⁶ When they have been characterized by Mössbauer spectroscopy, XANES, or X-ray photoelectron spectroscopy, however, BCFO samples prepared with a wide range of Ca contents in air at 1 atm pressure have been found to contain only Fe^{III}.^{4,10,17–19} The clear implication is that the substitution mechanism for the BCFO phases described here

Received: September 3, 2013

Revised: October 4, 2013

Published: October 7, 2013

and in the literature involves charge compensation by oxygen vacancies. In this case, the relevant end member phase is $\text{CaFeO}_{2.5}$, which has the brownmillerite structure and is orthorhombic ($Pnma$, $2a_p^{1/2} \times 4a_p \times 2a_p^{1/2}$) with an ordered arrangement of oxygen vacancies such that there are planes of FeO_4 tetrahedra and FeO_6 octahedra perpendicular to the crystallographic b axis (e.g., see Figure 1 of Ross et al.²⁰ or Figure 1a of Krüger et al.²¹). Octahedra within the FeO_6 layers are tilted, and the additional doubling of the unit cell, with respect to the conventional $Pnma$ perovskite structure, is due to the vacancy ordering. $\text{CaFeO}_{2.5}$ becomes antiferromagnetic below $T_N \sim 720$ K.^{22,23} It also has a structural phase transition between ~ 950 and ~ 1000 K to an incommensurate structure with a change in configuration of the tetrahedral layers and a change in tilting of the octahedral layers.^{21,24–26} There is some evidence for a possible additional transition at ~ 1310 K.²³

Figure 1 contains a collation of data from the literature relating to specific transitions and structure types across the

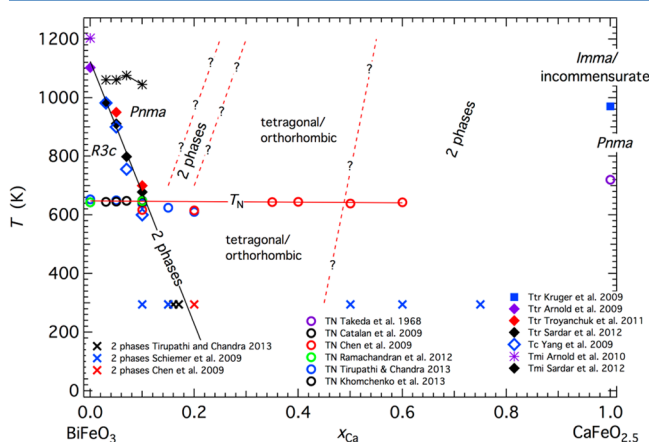


Figure 1. Subsolidus phase relations for the BiFeO_3 – $\text{CaFeO}_{2.5}$ solid solution. T_N represents Néel points, T_{tr} represents structural transition points, T_c represents the Curie temperature for the appearance of the ferroelectric structure, and T_{mi} represents a metal–insulator transition. The horizontal line is a fit to the data of Chen et al.⁷ for the T_N value of samples with compositions in the range $x = 0.35$ – 0.6 . The steep line at Ca-poor compositions is a fit to the data of Sardar et al.¹⁹ for the $R3c$ – $Pnma$ structural transition.

entire BiFeO_3 – $\text{CaFeO}_{2.5}$ solid solution. The topology at the BFO-rich end is similar to that proposed for thin films.²⁷ Increasing temperature and doping with Ca first cause the $R3c$ structure ($2a_p^{1/2} \times 2a_p^{1/2} \times 2(3a_p)^{1/2}$ in hexagonal setting, ferroelectric plus R-point tilting of FeO_6 octahedra) to undergo a first-order transition to the $Pnma$ structure (R- and M-point tilting^{5,19,28–30}). This occurs at ~ 1100 K in BFO but reduces in temperature with increasing Ca content and involves a significant interval (10 s of degrees) of coexisting phases. The structural transition temperatures of bulk samples correlate closely with the Curie temperatures reported for thin films.^{19,27} At higher temperatures, there is a metal–insulator transition, but this appears to not involve any change in crystallographic symmetry.³¹ T_N for BFO is ~ 643 K,³² and data from the literature are largely consistent with a slight increase to ~ 649 K at $x = 0.1$.³³

The pattern of transitions shown in Figure 1 at high temperatures for the BFO end of the solid solution seems to be well established, but the evolution of structure types with increasing Ca content at room temperature is less clear. There

is general agreement that there are coexisting phases in samples with bulk compositions that have x between ~ 0.1 and ~ 0.2 , but fits of powder diffraction data to structures with $Imma$ ($2a_p^{1/2} \times 2a_p \times 2a_p^{1/2}$) and $Pbam$ ($2a_p^{1/2} \times 2(2a_p)^{1/2} \times 2a_p$) and triclinic ($a_p \times a_p \times a_p$) symmetry have also been reported.^{4,5,30} Schiemer et al.¹⁸ reported two phases at $x = 0.1$, one of which was metrically rhombohedral and the second metrically cubic, but also found evidence for other structure types with different superlattice repeats by electron diffraction. Extrapolation of a linear fit to reported transition temperatures in the low Ca-doping range is directly into this two-phase region, and it seems likely that the additional phases are related to the onset of oxygen-vacancy ordering and that the variability reflects at least a degree of nonequilibrium from different sample preparation conditions and cooling rates. Phase boundaries for the appearance of ordered phases have not yet been established, but heating of a sample with $x = 0.2$ to temperatures above 350 °C after previously being quenched from much higher temperatures caused separation into two structures with different compositions.⁷ This single result is used in Figure 1 as a first guess for where the equilibrium cation/oxygen/vacancy ordering field might be approximately located.

At intermediate compositions ($0.2 < x < 0.5$), the BCFO solid solution has a field of stability for a structure with cation and oxygen/vacancy ordering.^{7,17,18} Currently, there is some inconsistency relating to details of the structure of bulk samples, however. On the basis of powder diffraction data, Chen et al.⁷ reported metrically cubic lattice geometry across the entire composition range, but metrically tetragonal dimensions were found at Ca-rich compositions by Schiemer et al.¹⁸ Lepoittevin et al.¹⁷ obtained an orthorhombic fit for a sample with $x = 0.5$. Electron diffraction reveals a superlattice repeat that is incommensurate ($2a_p \times 2a_p \times na_p$, $n \approx 5.5$ at $x = 0.2$ to $n \approx 4$ at $x = 0.5$) in the samples of Schiemer et al.¹⁸ and commensurate ($n = 8$, fringe spacing 4) in the sample of Lepoittevin et al.¹⁷ Chen et al.⁷ reported commensurate superlattice repeats of $\times 5$ and $\times 8$ in samples with $x = 0.33$ and 0.2 , respectively, but found substantial local variability and did not characterize the full lattice geometry. Models of the structure have blocks of perovskite containing FeO_6 octahedra alternating with layers containing Fe in square pyramidal (FeO_5) and tetrahedral (FeO_4) coordination because of ordering of the oxygen vacancies. There is, as yet, no information available in relation to whether octahedra in the perovskite layers are tilted. Lepoittevin et al.¹⁷ attempted a structure refinement under the orthorhombic space group $Bmmm$, but this was only one of a number of possibilities.

Individual samples with compositions in the intermediate range contain abundant twinning on an electron optical scale.^{17,18} With respect to a parent cubic structure, it is inevitable that the boundaries between at least some of these would be twin walls with ferroelastic character. A two-phase field of the intermediate ordered structure plus $\text{CaFeO}_{2.5}$ extends from $x \approx 0.5$.¹⁸ There are no experimental results available that might indicate ordering transition temperatures for any compositions of the intermediate phase, but these could be above the synthesis temperatures, which are usually ~ 900 – 950 °C. If this is correct, then the observed transformation-related microstructures must develop during growth and annealing of the polycrystalline samples.

Definitive determination of ferroelectricity is restricted to the rhombohedral structure. Chen et al.⁶ claim to have obtained a ferroelectric hysteresis loop from a sample with $x = 0.3$,

however. They did not report the structure type of their sample, but their conclusions suggest that it is possible that the intermediate structure could become ferroelectric. Attempts by Schiemer et al.¹⁸ to obtain saturated ferroelectric loops for a wider range of compositions were not successful, likely because of high intrinsic conductivity. Conventional analysis of the real and imaginary components of the dielectric response at frequencies between ~ 1 Hz and 10 MHz reveals loss behavior that can be characterized in terms of Arrhenius behavior. Reported values of the activation energy, E_a , are 0.3 eV for $x = 0.5$,¹⁷ 0.22 eV for $x = 0.36$,¹⁸ 0.42–0.27 for $x = 0.33$ –0.6,⁷ and ~ 0.65 eV for $x = 0.2$.³⁴ These values are generally discussed in the context of a mechanism involving mobile oxygen vacancies, which has been confirmed by a study of the influence of oxygen fugacity.³⁵

Strain Analysis and Order Parameter Coupling. The critical property in the context of elastic and anelastic behavior is strain. Figure 2 shows shear strains, as defined with respect to

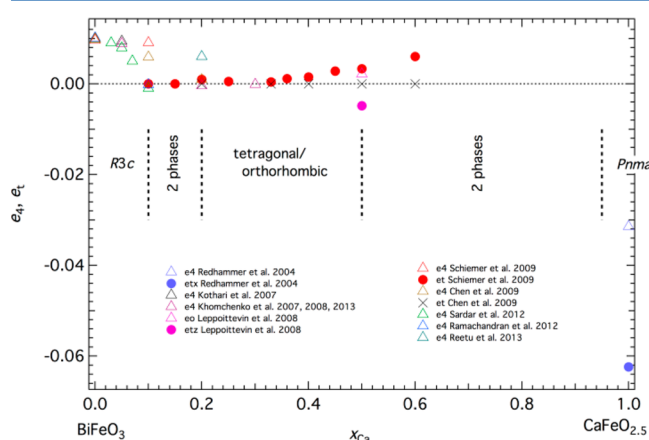


Figure 2. Variation of shear strains, defined with respect to a parent cubic structure, for members of the BFO–CFO solid solution as determined from lattice parameter data collected at room temperature.

a parent cubic reference state, at room temperature for each of the structure types at different compositions across the BCFO solid solution. These were obtained from lattice parameters in the usual way for spontaneous strains associated with phase transitions.³⁶ In principle, the symmetry of BFO is reduced to monoclinic if the magnetic cycloid ordering scheme has only one out of the three possible symmetry-related directions of the rhombohedral structure³ or if it is replaced by a weakly ferromagnetic scheme in which the sublattice magnetizations are oriented in the (111) plane.³⁷ A very small monoclinic distortion has been reported for some samples by Sosnowska et al.,³⁸ whereas Wang et al.³⁹ favored triclinic lattice geometry. The dominant nonzero shear strain at low Ca contents is e_4 , which is given by $e_4 \approx \cos\alpha$, where α is the rhombohedral lattice angle. In a tetragonal structure, the shear strain is $e_{tz} = 1/(3(2e_3 - e_1 - e_2))^{1/2}$, where $e_1 = e_2 = (a_p - a_0)/a_0$ and $e_3 = (c_p - a_0)/a_0$. In the absence of data for the parent cubic structure, a_0 is estimated as $a_0 = (a_p^2 c_p)^{1/3}$. Nonzero shear strains of the *Pnma* structure are e_4 and e_{tz} , for which expressions in terms of the lattice parameters are given by McKnight et al.⁴⁰ A clear pattern shown by Figure 2 is that the shear strains at room temperature reduce slightly with increasing Ca content across the *R3c* field and are close to zero at Ca-rich compositions in the intermediate phase (or strictly zero if the lattice geometry is cubic) but increase toward $x = 0.5$. There is a very obvious first-

order discontinuity in e_4 near $x = 0.1$. Coupling of shear strains with the order parameter for cation/oxygen/vacancy ordering clearly varies with composition, but the shear strains of $\text{CaFeO}_{2.5}$ do not match up with this pattern in that they are large and have opposite sign. There are no data for the lattice parameter of a high-temperature parent cubic structure at any compositions, so it is not possible to determine the extent of coupling with volume strain.

Changes in magnetic structure accompany variations in structure type across the solid solution. Remarkably, however, the Néel temperature barely changes (Figure 1), and the evolution of the antiferromagnetic order parameter also follows a very similar temperature dependence at compositions between $x = 0$ and 0.6.⁷ There are slight variations in magnetic structure, but the basic ordering scheme is believed to be G-type antiferromagnetic at all compositions.⁷ Pure BFO is antiferromagnetic with a cycloid structure.^{3,41,42} Ca-doped rhombohedral samples are weakly ferromagnetic, which is attributed to canting allowed by symmetry if the cycloid is suppressed.^{4,5,7,10,37,43} The intermediate phases ($x \approx 0.2$ –0.5, tetragonal or orthorhombic) are antiferromagnetic.^{7,18,34,44–46}

With respect to strain coupling, a small change occurs in the trend of the rhombohedral lattice angle of BFO between ~ 650 and ~ 800 K in BFO⁴⁷ and is also just about visible in the data shown in Figure 8 of Sardar et al.¹⁹ for samples with $x = 0.03$ and 0.05. Even if this is due to coupling with the antiferromagnetic order parameter, the total shear strain is clearly very small. However, there is a distinct break in slope of the a (pseudocubic) lattice parameter and unit cell volume at ~ 650 K in both sets of data, implying a negative volume strain that amounts to $\leq \sim -0.001$ at 300 K. The most recent lattice parameter determination⁴⁸ is also consistent with these small strain variations. In other words, there is weak coupling of the magnetic order parameter(s) to volume strain. No equivalent data are yet available for more Ca-rich compositions, but the expectation is that coupling with shear strains will also be weak/negligible and only weak with the volume strain. These views, which are based on empirical data, are also entirely consistent with the conclusions of Ederer and Spaldin,⁴⁹ which are based on first principles density functional calculations, that ferroelectric polarization in BFO is insensitive to strain and the presence of oxygen vacancies. They found also that magnetization is unaffected by strain but the introduction of vacancies can alter it slightly.

The phase diagram and strain data in Figures 1 and 2 provide constraints on the overall coupling behavior of ferroic and multiferroic phases in the BCFO solid solution. First, magnetic ordering occurs below an almost constant Néel temperature and follows the same temperature dependence, irrespective of crystallographic structure, cation/oxygen/vacancy ordering, ferroelectric order, or ferroelastic (shear) strain. From this, it can be concluded that the antiferromagnetic order parameter does not couple, or couples only very weakly, with order parameters relating to the other processes. Independent confirmation of weak and unfavorable coupling between ferroelectric and magnetic order parameters has also been provided by observations of Fe and Bi displacements as a function of temperature in BFO.⁴⁸ Furthermore, the only detectable coupling of the magnetic order parameter with strain is restricted to volume strains. There must be subtle structural/chemical influences which favor cycloidal, weakly ferromagnetic, or purely antiferromagnetic ordering schemes, but this can be only a very minor variation. Second, ferroelectric

ordering appears to be restricted to the rhombohedral structure. In BFO with low Ca-doping, there must be a balance between competing R- and M-point octahedral tilting, which would favor *Pnma*, and ferroelectric displacements coupling with R-point tilting, which favors *R3c*. This balance favors *Pnma* with the addition of Ca. At high enough vacancy concentrations, the tilting and ferroelectric order parameters become overwhelmed by the cation/oxygen/vacancy ordering. Third, there are significant but different ferroelastic shear strains in all of the reported structures. Tilting plus ferroelectric displacements gives strains of up to $\sim 1\%$ in the rhombohedral structures. The intermediate structure has smaller shear strains of up to ~ 0.006 , which are most likely due predominantly to coupling with the cation/oxygen/vacancy ordering. The much larger shear strains of $\text{CaFeO}_{2.5}$, up to 6%, and their opposite sign serve to indicate that although the entire solid solution depends on charge balancing by oxygen vacancies, details of the brownmillerite structure and of the intermediate structure must be significantly different.

Finally, all members of the BCFO solid solution develop transformation-related microstructures. Twin walls are known to interact strongly with oxygen vacancies as seen, for example, in $(\text{Ca,Sr})\text{TiO}_3$ and LaAlO_3 .^{50–55} It seems inevitable that twin walls must also interact with oxygen vacancies in the intermediate structure of BCFO. This has implications for both dielectric and acoustic loss as well as for switching in addition to the expected influence of the vacancies on electrical conductivity. In particular, movement of oxygen vacancies under an applied electric field will inevitably give rise to local strains, from which it follows that acoustic and dielectric loss properties should be closely related. It has also been suggested³⁰ that the domain walls might have locally different magnetic states.

■ EXPERIMENTAL SECTION

Synthesis. The sample investigated was of nominal composition $\text{Bi}_{0.64}\text{Ca}_{0.36}\text{FeO}_{2.82}$ (BCFO 36) and was from the same batch used in Schiemer et al.¹⁸ This sample was prepared by a rapid two-stage reaction method using high-purity Bi_2O_3 , CaCO_3 , and Fe_2O_3 powders. The starting powders were first homogenized for ~ 20 min in an agate mortar before calcination at 850°C for 20 min. The sample was then reground for a further 20 min, pressed into a pellet at 480 MPa in a 13 mm diameter cylindrical uniaxial steel die, and sintered at 990°C for 20 min. This sample showed no secondary phases from XRD or SEM examination, although some local inhomogeneity (on the order of 1% composition) was seen in back-scattering mode and via EDX in the SEM, as described in Schiemer et al.¹⁸ The resultant pellet was cut into a rectangular parallelepiped for RUS measurement using an annular diamond saw. The measured dimensions, $4.229 \times 2.703 \times 1.812\text{ mm}^3$, and mass 0.1349 g, give an estimated density of 6.513 g cm^{-3} . Comparison of this with a theoretical density of 6.891 g cm^{-3} , as calculated using lattice parameter data of Schiemer et al.,¹⁸ implies a porosity of 5.5%.

RUS. The RUS method has been described in detail elsewhere.⁵⁶ In Cambridge, spectra are routinely collected using in-house built room-temperature, low-temperature, and high-temperature RUS heads. Room-temperature spectra were collected with the sample held directly between the piezoelectric (PZT) transducers across pairs of corners, pairs of edges, and pairs of faces. Values of the shear (G) and bulk (K) moduli were then determined by fitting to the frequencies of resonance peaks with the software described by Migliori and Sarrao.⁵⁶

Low-temperature RUS data were collected using dynamic resonance system (DRS) “modulus II” electronics and an Orange helium-flow cryostat, as described by McKnight et al.⁵⁷ The sample was held across a pair of faces directly between the transducers. The automated sequence involved collection of spectra at 30 K intervals during

cooling from ~ 280 to ~ 10 K, with a period of 20 min allowed for thermal equilibration before data collection. This was followed by heating between ~ 10 and ~ 305 K, with data collection at 5 K intervals and the same thermal equilibration period at each temperature. Each spectrum contained 65 000 data points in the frequency range 50–1200 kHz. Measured temperatures are believed to be accurate to within ± 1 K, and temperature stability during data collection is better than ± 0.1 K.

High-temperature spectra were collected with the sample balanced across a pair of corners between the tips of two alumina rods protruding into a horizontal tube furnace. In this system, the transducers are on the ends of the rods, outside the furnace, as described by McKnight et al.,⁵⁸ and spectra are collected using Stanford electronics.⁵⁹ Temperature is monitored by a thermocouple sited within a few millimeters of the sample and checked from time to time against the α – β transition temperature of quartz, giving an experimental uncertainty of ± 1 K. Spectra were collected in heating and cooling sequences between 295 and ~ 810 K, with ~ 20 K steps during heating and ~ 10 K steps during cooling. A period of 20 min was again allowed for thermal equilibration at each temperature. Individual spectra contained 65 000 data points in the frequency range 100–1200 kHz.

Raw spectra were transferred to the software package Igor (WaveMetrics) for analysis. Selected peaks were fit with an asymmetric Lorentzian function to determine their peak frequencies, f_0 , and width at half-maximum height, Δf . Each resonance mode depends on some combination of elastic constants that scales with f^2 . Because individual resonances are dominated by shearing, with generally small contributions from breathing modes, they provide information mainly relating to the shear modulus when the sample is polycrystalline. Acoustic loss is measured in terms of the mechanical quality factor, Q , which is usually determined as $Q^{-1} = \Delta f/f_0$.

Electrical Spectroscopy. Dielectric properties have already been collected on a different sample from the same material as was used for RUS measurements in the present study. These were collected using a high-precision LCR meter (Agilent 4284A), as described more fully in Schiemer et al.¹⁸ Impedance measurements were collected on a high-temperature measurement system (Xian Jiaotong University, China) via a precision LCR meter (Agilent, E4980A).

Magnetism. Remnant magnetization measurements were made on the same sample as used for the RUS measurements in a MPMS XL SQUID magnetometer. The magnetic moment was collected in zero applied field during a heating sequence from 5 K to room temperature.

■ RESULTS

Room Temperature. Table 1 gives values of the bulk and shear moduli obtained from fitting to the frequencies of 39

Table 1. Values of the Bulk and Shear Moduli Determined in the Present Study in Comparison with Data from the Literature, Including Voigt–Reuss–Hill Averages of Single-Crystal Data Given by Ruello et al.⁶² for BiFeO_3

sample	K (GPa)	G (GPa)
BCFO 36	95.7 ± 0.7	52.7 ± 0.1
BCFO 36, corrected for 5.5% porosity	109.0	58.6
BFO, Voigt–Reuss–Hill average	112.0	40.8
BFO, Zhu et al. ⁶³	97.3	
$\text{Bi}_{0.9}\text{Nd}_{0.1}\text{FeO}_3$, Schiemer et al. ⁶⁴	105.0	45.1
$\text{Bi}_{0.9}\text{Sm}_{0.1}\text{FeO}_3$, Schiemer et al. ⁶⁴	115.4	48.5

peaks measured at room temperature. The rms error for the fit was 0.25%. Also given are values corrected for porosity using the expressions of Ledbetter et al.⁶⁰ Literature data for these types of materials are sparse, but single-crystal values for BiFeO_3 (BFO) have been calculated from first principles⁶¹ and partially validated experimentally.⁶² Voigt–Reuss–Hill averages

of the preferred set given by Ruello et al.⁶² are listed in Table 1. There is also a single measurement of K as 97.3 GPa for BFO from equation-of-state measurements.⁶³ Bulk and shear moduli of polycrystalline samples of $\text{Bi}_{0.9}\text{Ln}_{0.1}\text{FeO}_3$ ($\text{Ln} = \text{Nd, Sm}$) were previously measured by RUS,⁶⁴ and values corrected for porosity confirm that K for all of these materials is in the range ~ 100 – 115 GPa, whereas the shear modulus of BCFO 36 is distinctly higher than for BFO or BFO with a small amount of the second component in solid solution.

Low Temperatures. Segments of the low-temperature spectra are shown in Figure 3, stacked in proportion to the

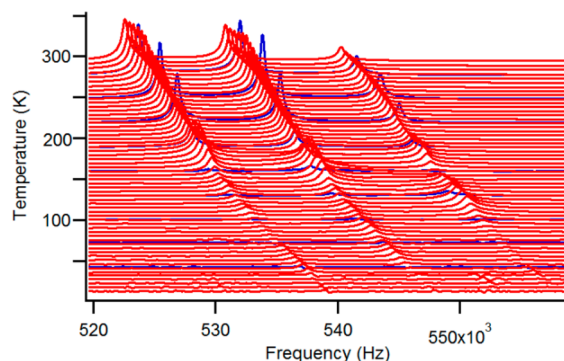


Figure 3. Segments of RUS spectra from the low temperature instrument. The y axis is amplitude in volts, but each spectrum has been offset in proportion to the temperature at which it was collected and the axis is labeled as temperature. Blue traces are spectra collected during cooling, and red traces are spectra collected during heating.

temperatures at which they were collected. They show a trend of increasing frequency of individual resonances (elastic stiffening) with falling temperature, as might generally be expected, except that there is clearly a subtle change in trend below ~ 150 K. This change in trend is confirmed in frequency data from two resonance peaks, as shown in Figure 4. The square of the resonance frequency scales predominantly with the shear modulus, G , and has a steeper slope below ~ 130 K than above. Not so evident in the raw spectra, however, is a broad peak in Q^{-1} below ~ 200 K and centered near 100 K.

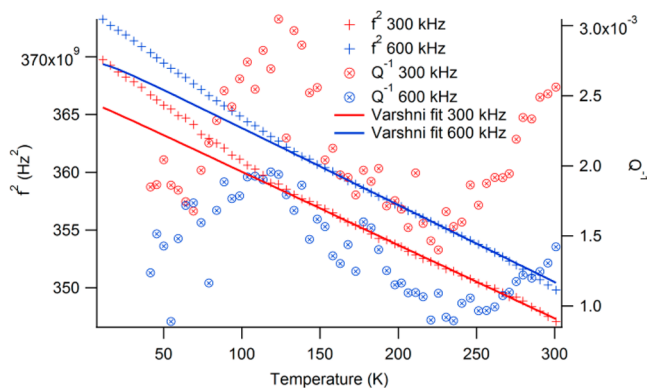


Figure 4. Data from fitting of two resonance peaks, near 300 and 600 kHz, in low-temperature spectra. f^2 values for the 300 kHz peak have been rescaled to roughly match the value for the 600 kHz. Lines are fits to the data for f^2 in the temperature interval ~ 145 – 300 K using eq 1 (300 kHz: $f_0 = 8.317 \times 10^{10} \text{ Hz}^2$, $S = 2.17 \times 10^8 \text{ Hz}^2$, $t = 15.05 \text{ K}$; 600 kHz: $f_0 = 3.695 \times 10^{11} \text{ Hz}^2$, $S = 2.17 \times 10^9 \text{ Hz}^2$, $t = 32.44 \text{ K}$).

The temperature dependence of the shear modulus is expected to have zero slope as $T \rightarrow 0 \text{ K}$, as represented by the Varshni equation for single-crystal elastic constants, c_{ij}

$$c_{ij} = c_{ij}^0 - \frac{S}{(e^{t/T} - 1)} \quad (1)$$

where c_{ij}^0 is the value of the elastic constant at 0 K and S and t are constants.⁶⁵ Fits of this to data in the temperature interval ~ 145 – 300 K are shown in Figure 4. The extrapolation to 0 K reveals the nature of the anomaly as being a marked but small (up to $\sim 2\%$) amount of stiffening of the shear modulus below $\sim 130 \text{ K}$.

If they are directly related, then the elastic stiffening below $\sim 130 \text{ K}$ and the peak in Q^{-1} are indicative of some thermally activated strain-relaxation process. In this case, a single Debye peak in Q^{-1} measured as a function of temperature at constant frequency can be described by

$$Q^{-1}(T) = Q_m^{-1} \left[\cosh \left\{ \frac{E_a}{kr_2(\beta)} \left(\frac{1}{T} - \frac{1}{T_m} \right) \right\} \right]^{-1} \quad (2)$$

where Q_m^{-1} is the maximum value of the loss within the peak, E_a is the activation energy, k is the Boltzmann constant, $r_2(\beta)$ is a parameter that reflects the width of a Gaussian spread in the relaxation times, and T_m is the temperature at which the mechanical losses are maximal.^{66,67} Following Carpenter et al.⁶⁸ and Thomson et al.,⁶⁹ eq 2 was initially fit to variations of Q^{-1} that are in excess of a linear baseline (Figure 5) using $r_2(\beta) = 1$ and giving fit parameters $T_m = 108 \text{ K}$, $Q_m^{-1} = 7.95 \times 10^{-4}$, and $E_a = 0.022 \text{ eV}$ for the 600 kHz Q^{-1} data. A single relaxation process ($r_2(\beta) = 1$) with a fixed activation energy would also be expected to give loss peaks at different temperatures, depending on the measuring frequency according to (from eqs 3.5–5 of Norwick and Berry⁷⁰):

$$\ln \left(\frac{\omega_2}{\omega_1} \right) = \frac{E_a}{k} \left(\frac{1}{T_{m1}} - \frac{1}{T_{m2}} \right) \quad (3)$$

Here, T_{m1} and T_{m2} are the temperatures of maxima in Q^{-1} as measured at frequencies ω_1 and ω_2 ($\omega = 2\pi f$). The initial value of 0.022 eV for E_a gives T_{m2} as being $\sim 155 \text{ K}$ higher than T_{m1} when measured at 900 kHz, rather than 300 kHz, which is clearly incorrect. The activation energy of 0.22 eV extracted from dielectric loss data in a similar temperature range (Schiemer et al.,¹⁸ and see below) has therefore been fixed in a separate fitting of the acoustic loss peaks, and this gives $r_2(\beta) \approx 5.5$ at different frequencies (Figure 5).

Dielectric data presented in Figure 11 of Schiemer et al.¹⁸ (1 kHz to 1 MHz, 100–180 K) show a pronounced, frequency-dependent loss peak, and room-temperature measurements are consistent with a classic Debye pattern. Standard Arrhenius treatment using the frequencies at which the dielectric loss was at a maximum also showed that the data can be well represented by a single-relaxation process following

$$f = f_0 e^{-E_a/kT_m} \quad (4)$$

with $E_a = 0.22 \text{ eV}$ and $f_0 = 1.89 \times 10^{14} \text{ Hz}$. The temperature dependence of the dielectric loss at 300 and 800 kHz is reproduced in Figure 6 to show that it is essentially indistinguishable in form from the acoustic loss measured at almost the same frequencies. Figure 7 is an equivalent plot

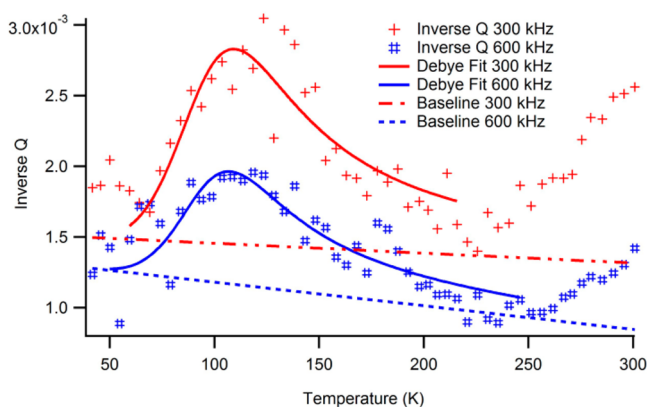


Figure 5. Fits to Q^{-1} data from Figure 4 using eq 2 to represent the increase in loss above linear baselines. $E_a = 0.22$ eV (fixed). $T_m = 109.5$, $Q_m^{-1} = 0.00138$, and $r_2(\beta) = 5.841$ (300 kHz); $T_m = 107.9$, $Q_m^{-1} = 0.00080$, and $r_2(\beta) = 5.413$ (600 kHz).

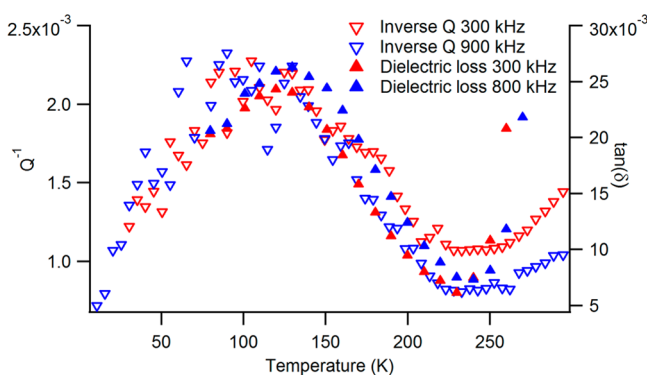


Figure 6. Comparison of the inverse quality factor of two selected peaks from RUS data of BCFO 36 (this study) with the dielectric loss measured at similar frequencies (data from Schiemer et al.¹⁸).

comparing dielectric permittivity with elastic compliance ($1/f^2$), and again the two sets of data are closely similar in form.

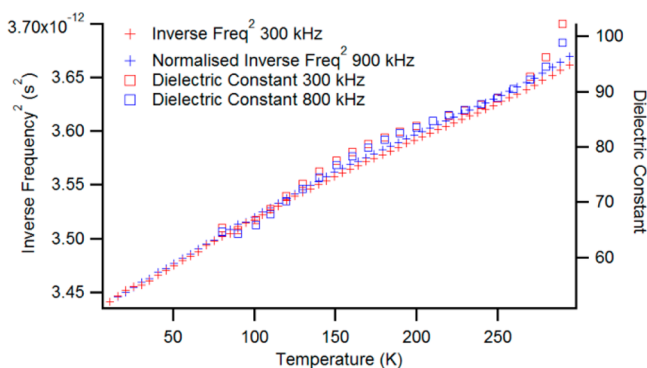


Figure 7. Comparison of $1/f^2$ data from RUS (this study) with dielectric permittivity measured at about the same frequencies (data from Schiemer et al.¹⁸).

Values of K and G from fitting with 35–40 resonance peaks (with rms errors of 0.24–0.3%) are shown in Figure 8. The scatter in the data is too great to determine whether the break in slope of G near 130 K occurs also in K , but they are adequate to yield temperature dependences below temperature of $dK/dT = -12.22$ MPa K^{-1} and $dG/dT = -12.248$ MPa K^{-1} .

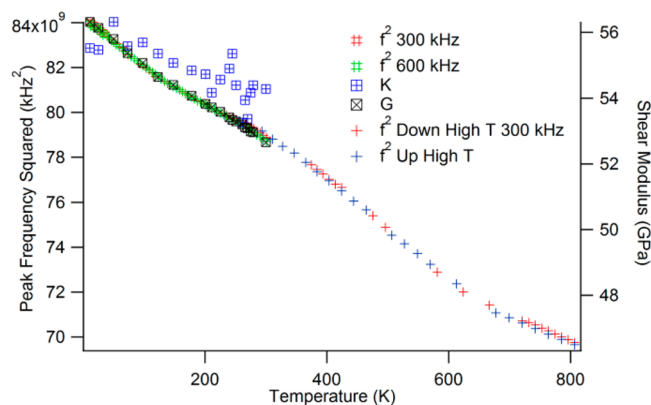


Figure 8. Variations of the absolute values of the bulk, K , and shear, G , moduli below room temperature as well as the squared peak frequencies at high temperature, predicting the trends in the shear modulus above room temperature. K has been scaled to roughly coincide with G for ease of viewing.

After cooling from ~ 800 K to room temperature in the furnace used for high-temperature RUS measurements and then down to 5 K in zero field in the SQUID magnetometer, the BCFO sample had a magnetic moment of $\sim 2 \times 10^{-6}$ emu. As shown in Figure 9, there were no obvious changes in

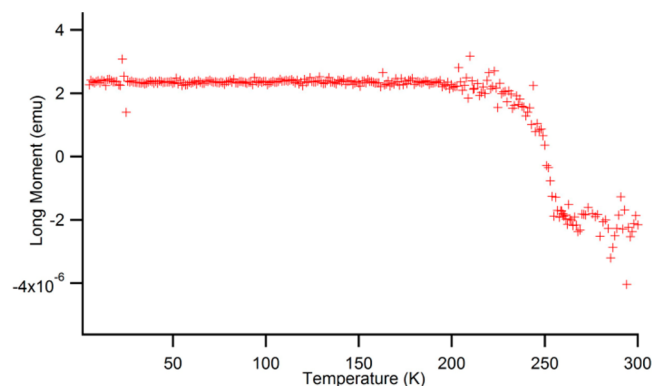


Figure 9. Magnetic moment data as a function of temperature obtained during heating in zero applied field. The anomaly near 250 K is assumed to be due to the Morin transition in a small amount of hematite present as an impurity phase.

moment during heating to ~ 220 K, but a smooth and relatively steep anomaly occurred between ~ 220 and 250 K. The form of the anomaly closely resembles that shown by hematite, Fe_2O_3 , which has a first-order transition from antiferromagnetic below the Morin transition at ~ 260 K to weakly ferromagnetic (canted antiferromagnet) above it. The change in moment observed here is ~ 1000 times smaller than obtained for a polycrystalline RUS sample of hematite (+ $\sim 3\%$ magnetite) with similar dimensions to the sample used in the present study (see Figure 8 of Oravova et al.⁷¹). It seems likely, therefore, that the magnetic measurements indicate the presence of some trace amount of hematite as an impurity phase. There is no overt evidence in the data that BCFO 36 itself undergoes significant changes in magnetic structure below room temperature.

High Temperatures. Figure 10 contains segments of spectra from the high-temperature instrument, stacked in proportion to the temperature at which they were collected. These show a break in trend of the peak frequencies and a marked increase in linewidths below ~ 650 – 700 K, as

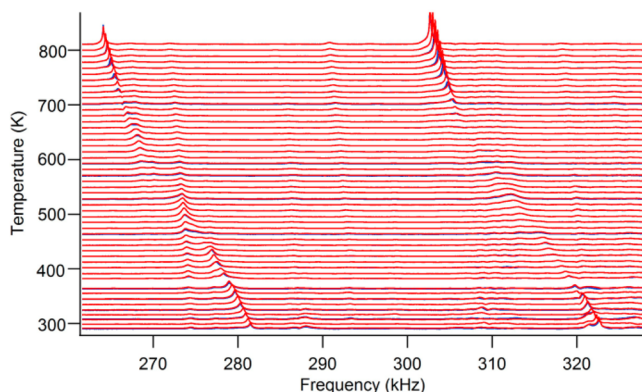


Figure 10. Segments of RUS spectra from the high-temperature instrument. The y axis is amplitude in volts, but each spectrum has been offset in proportion to the temperature at which it was collected and the axis is labeled as temperature. Spectra shown in blue were collected during heating, and those in red, during cooling. Resonance peaks with frequencies that vary only weakly with temperature are from the alumina buffer rods.

quantified by data for f^2 and Q^{-1} from fitting of the two peaks (Figure 11). Also shown is the Néel temperature (~ 645 K) for

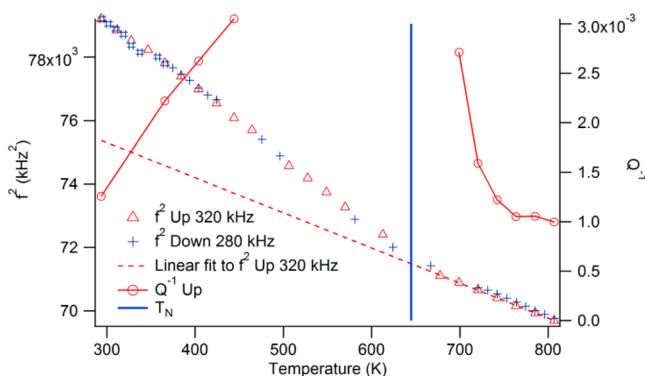


Figure 11. Data from fitting of two resonance peaks, near 280 and 320 kHz, in high-temperature RUS spectra. f^2 values for the 320 kHz peak have been rescaled to match the value for the 280 kHz peak at 295 K. The vertical line shows $T_N = 645$ K for BCFO 40 from Chen et al.⁷

a sample with $x = 0.4$, taken from Figure 9 of Chen et al.⁷ This nearly coincides with the break in slope of frequency with temperature and falls just below the onset in the steep rise in Q^{-1} .

Complex impedance data have been collected between room temperature and 700 K. They are shown here in Figure 12. Highly capacitive behavior is seen, as expected, at room temperature, with resistivity of 10^2 – 10^3 Ω m and reactance of -10^1 – 10^2 Ω m and a frequency dependent peak in the resistivity near 350 K. The resistivity drops sharply to ~ 1 Ω m by ~ 450 K, at which point it plateaus and develops a frequency dispersion. This anomaly persists until ~ 525 K, above which the resistivity continues to drop, with a low value of $\sim 10^{-1}$ Ω m at 700 K. By 400 K, the reactance has increased to $\sim -10^{-1}$ Ω m, and above the anomalous region, from 550 K, the reactance is slightly positive ($\sim 10^{-2}$ – 10^{-1} Ω m), indicating inductive, rather than capacitive, behavior and suggesting that the material has become a conductor. Attempting to examine this in terms of thermally activated Arrhenius behavior yields the information in Figure 13. This shows that two distinct regions of slope exist,

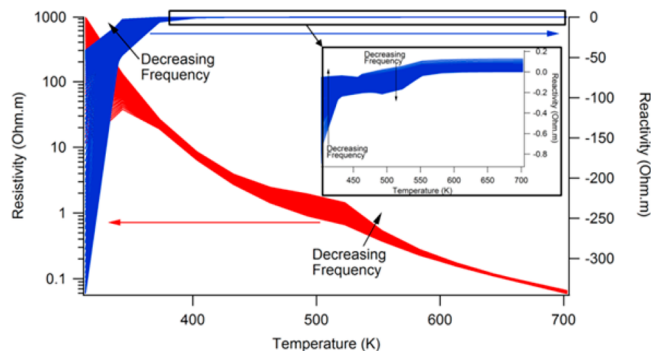


Figure 12. Complex impedance at high temperatures measured at a range of frequencies between 20 Hz and 2 MHz. The inset shows the reactance behavior from 400 K and up.

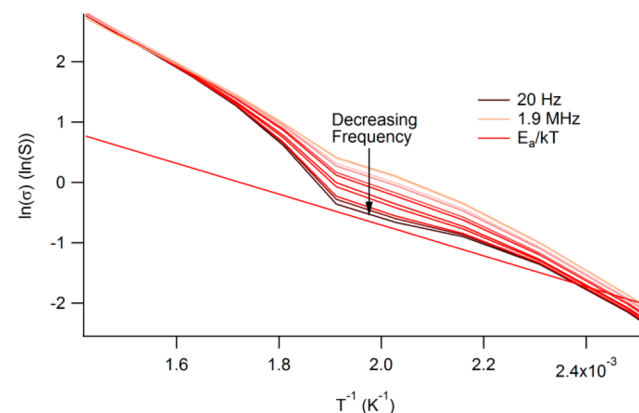


Figure 13. Arrhenius plot of resistance, at high temperatures measured at a range of frequencies between 20 Hz and 2 MHz. The line shows the fit expected from an activation energy of 0.22 eV, as discussed previously.

typical of the behavior of doped semiconductors, with the region on the right related to the thermal activation of extrinsic dopant charge carriers and the region on the left related to intrinsic conductivity. There is a marked frequency dispersion in the transition region at around 500 K. The line shown on the figure is that of a linear fit to E_a/kT with activation energy of 0.22 eV, as previously found by Schiemer et al.¹⁸ for this system at low temperature. This gives a reasonable fit for the lower-temperature slope, suggesting that the transition region occurs as all oxygen vacancies become thermally activated.

DISCUSSION

Patterns of phase transitions across the phase diagram, the spontaneous strains that accompany changes in structural state, anomalies in the elastic and anelastic properties of BCFO 36, and correlations between elastic behavior and dielectric behavior are all revealing of the nature and strength of coupling between the multiple order parameters that operate in BFO–CFO. These are due to octahedral tilting, q , cation/oxygen/vacancy ordering, q_{od} , ferroelectric polarization, p , and antiferromagnetic ordering, m . The nonzero strains couple with each order parameter as λeq^2 , λeq_{od}^2 , λep^2 , and λem^2 , whereas coupling between the order parameters themselves, either directly or indirectly through common strains, is biquadratic (i.e., $\lambda q^2 q_{od}^2$, $\lambda q^2 p^2$, $\lambda q^2 m^2$, $\lambda q_{od}^2 p^2$, $\lambda q_{od}^2 m^2$, and $\lambda p^2 m^2$). Two separate tilt order parameters, q_R and q_M , relate to R- and M-point tilting schemes. Possible patterns of structural

evolution in systems with two instabilities and biquadratic coupling between the order parameters have been set out by Salje and Devarajan.⁷² The most general characteristic behavior when the order parameters are able to relax on a fast time scale is of sequences of stability fields for different structures that may be separated by first- or second-order transitions. In the present system, however, it is unlikely that the degree of cation/oxygen/vacancy order re-equilibrates in response to changes in p , m , or q under laboratory time scales at temperatures less than ~ 1000 K. In this case, the influence of λq_{od}^2 is as an effective field that would renormalize the critical temperature of the instability to which it is coupled. In other words, samples with different degrees of cation/oxygen/vacancy order would be expected to have different magnetic, ferroelectric, and tilting transition temperatures.

Coupling between p and q stabilizes a ferroelectric structure with only one tilt system, with respect to one with two tilts (i.e., $\lambda q_{\text{R}}^2 p^2$ is probably favorable). The introduction of oxygen vacancies causes the ferroelectric structure to be suppressed, but if there is any cation/oxygen/vacancy ordering involved, then it is presumably restricted to a local length scale because there is no evidence for long-range ordering in the $Pnma$ structure. On the basis of very low shear strains in the intermediate structure, it appears that cation/oxygen/vacancy ordering suppresses tilting (i.e., $\lambda q^2 q_{\text{od}}^2$ terms are unfavorable). This contrasts with $\text{CaFeO}_{2.5}$ with its large shear strains and known tilting of octahedra in the perovskite layers. On this basis, incommensurate ordering appears to be incompatible with tilting.

In the absence of tilting, the lowering of symmetry from cubic to tetragonal or orthorhombic at intermediate compositions would likely be due to only ordering of cations and oxygen vacancies. Volume strains tend to be small for both tilting and cation ordering, with the result that the bulk modulus at room temperature is likely to be relatively insensitive to structural state. However, significant softening of the shear elastic constants accompanies tilting transitions. In LaAlO_3 , for example, the cubic \leftrightarrow rhombohedral transition results in a lowering of the shear modulus, G , by $\sim 25\%$ (Carpenter et al.⁵⁴). BFO has a significant shear strain at room temperature, whereas BCFO 36 is close to being metrically cubic. The shear modulus of BFO at room temperature could be as much as 30% softer than that of BCFO 36 (Table 1), and much of this is likely to be due to the tilting in the former and the lack of tilting in the latter.

All of the evidence from the phase diagram and the elasticity data presented here indicates that the magnetic order parameter is only weakly coupled with the other order parameters, if at all. In particular, T_{N} values are essentially independent of composition and structure type (Figure 1), and the antiferromagnetic order parameter, m , has almost exactly the same temperature dependence in phases with different compositions across the solid solution.⁷ In other words, the coupling coefficients for $\lambda q^2 m^2$, $\lambda q_{\text{od}}^2 m^2$, and $\lambda p^2 m^2$ must be small, and the latter has also been shown to be unfavorable.⁴⁸ The most likely explanation for this is, first, that any direct coupling is weak and, second, that m couples only very weakly with strain, e . Weak coupling between e and m means that the possibilities for indirect coupling with any other order parameters via common strains are strictly limited. The lack of coupling of m with shear strains is confirmed by the absence of softening of the shear modulus below T_{N} in BCFO 36 (this study) and also in $\text{Bi}_{0.9}\text{Nd}_{0.1}\text{FeO}_3$.⁶⁴ Elastic softening below the

transition point is typical of systems with linear-quadratic coupling ($\lambda e m^2$ here) if the order parameter (m) relaxes in response to an applied stress on the time scale of the measurement.^{73–75} From the discussion of strains above, it appears that there is a small volume strain associated with the magnetic ordering, in which case a small degree of softening of the bulk modulus is expected.

Biquadratic coupling of strains with an order parameter, $\lambda e^2 m^2$ in the present case, is always allowed by symmetry, and even a zero or very small shear strain e_i would cause a renormalization of the shear elastic constant, C_{ii} , according to $C_{ii} = C_{ii}^0 + 2\lambda m^2$, where C_{ii}^0 is the elastic constant of the paramagnetic phase extrapolated into the stability field of the antiferromagnetic phase. This is easily tested since the change in elastic properties becomes an excess, with respect to the para phase, which should scale with the square of the order parameter. The straight line shown in Figure 11 is a linear fit to data above T_{N} , representing the shear modulus of the paramagnetic phase of BCFO 36. Differences between this and the observed values of f^2 , Δf^2 , are shown in Figure 14

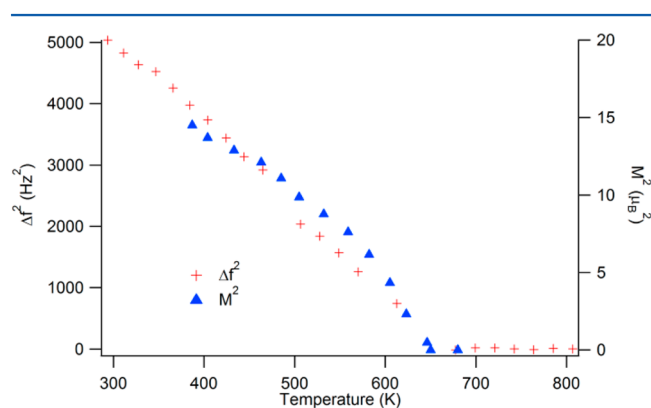


Figure 14. Comparison between Δf^2 from Figure 11 and the square of the magnetic order parameter for a sample with $x = 0.4$ from Figure 8 of Chen et al.⁷

along with values of m^2 extracted from the data for a sample with $x = 0.4$ from Figure 8 of Chen et al.⁷ Within experimental uncertainty, the overlapping trends confirm the existence and significance of biquadratic coupling between shear strains and the magnetic order parameter. There are no equivalent data available for m in $\text{Bi}_{0.9}\text{Nd}_{0.1}\text{FeO}_3$, but the same pattern of elastic stiffening was observed by Schiemer et al.⁶⁴

In marked contrast with the independence of T_{N} and the evolution of m with respect to ferroelectric behavior, octahedral tilting, and cation/oxygen/vacancy ordering, the crossover from a cycloidal antiferromagnetic ordering scheme to a commensurate scheme that is weakly ferromagnetic is highly sensitive to composition. The stability field of the cycloid does not extend very far into the solid solution because the room temperature structures at $x = 0.03$ display weak ferromagnetism;³⁰ its boundary does not appear to be coincident with any of the structural transitions. Macroscopic strains do not modify the antiferromagnetic G-type ordering of Fe^{III} moments, but local strain heterogeneity associated with replacing Bi^{III} ions (Shannon ionic radius 1.17 Å in 8-fold coordination) with Ca^{II} (1.12 Å in 8-fold coordination), with the resultant loss of the natural off-centering created by the Bi^{III} lone pair and the creation of oxygen vacancies, could provide the mechanism for disrupting the classic order parameter gradient coupling

required to stabilize an incommensurate structure. Strain fields around impurity atoms in oxide perovskites can be thought of as spheres of local distortion with radii of $\sim 8\text{--}9\text{ \AA}$ that effectively start to impinge on each other at a doping level of $\sim 1.5\%$.⁷⁶ The acoustic loss behavior discussed below provides evidence of strain relaxation around individual vacant oxygen sites, and this would presumably modify tilting and shearing of neighboring octahedra across the same length scale. The local state of oxide solid solutions, more generally, is also of overlapping strain fields, which gives rise to a degree of local heterogeneity that can be characterized by measurements of line broadening in infrared spectra.^{77–83} On this basis, the limit of stability of the cycloid ordering scheme would be expected to be at or below $\sim 1\%$ doping.

Acoustic losses occur in two temperature intervals and coincide at low temperature with dielectric losses measured at similar frequencies and at high temperature with anomalous conductivity behavior. The correlation between the dielectric and (an)elastic properties below room temperature is so close (Figures 6 and 7) that they must be due to essentially the same process driven either by an external electric field or by external stress. The description of the response to these fields in terms of thermally activated processes and the magnitude of the activation energy are consistent with the loss mechanism being related to the movement of oxygen vacancies. If the treatment is correct, it also implies a wide spread of relaxation times that, in turn, implies the oxygen vacancies involved are not in a uniform environment. Variations in environment could be due to local ordering/clustering and proximity to twin walls. As stated in the introduction above, variations in local potential between twin walls and uniform twin domains almost inevitably leads to energetically preferred locations for oxygen vacancies in perovskites. TEM observations confirm the existence of twin walls in the intermediate phase of BCFO,¹⁸ and given that the macroscopic symmetry is lower than cubic, some of these must inevitably be ferroelastic in character. However, walls between domains for which the difference is primarily due to cation or oxygen/vacancy ordering will not be mobile to anything like the extent expected for twin walls between domains where the difference is due to a displacive order parameter. For the moment, it is only possible to propose that there are a range of environments for oxygen vacancies in BCFO 36, that their movement involves a change in local dielectric properties and strain, and that freezing of this movement occurs in the temperature range $\sim 50\text{--}200\text{ K}$ at measuring frequencies of a few hundred kilohertz. Maximal losses occur near 100 K at these frequencies. Associated with the loss behavior are small changes in the shear elastic constant and the dielectric permittivity, indicating small differences in these properties between the unrelaxed states (high measuring frequencies) and the relaxed states (low measuring frequencies), according to the Debye relations.

Large acoustic losses and anomalous conductivity have been observed above $\sim 350\text{--}400\text{ K}$ (Figures 11 and 13) and, again, the correlation is permissive of a common loss mechanism. The overall pattern is consistent with increasing ionic conductivity with increasing temperature. Movement of oxygen ions and vacancies under the influence of an applied electric field will be coupled to local strain clouds. Conversely, therefore, application of a stress field can cause analogous displacements. There is no evidence from the elasticity measurements of a structural transition at $\sim 430\text{ K}$, so the onset of ionic conductivity is not obviously related to some specific change

in structural state. Q^{-1} for BCFO 36 is low at high temperatures but increases steeply below $\sim 750\text{ K}$ (Figure 11). This could perhaps include some acoustic loss behavior associated with the antiferromagnetic ordering, but it is still within a temperature interval of anomalous impedance (Figure 13) and could simply be a function of the dynamics of oxygen-vacancy mobility. Dielectric measurements on BFO with lower levels of Ca-doping show increasing loss above only $\sim 500\text{ K}$ and a pattern that could be more directly related to the magnetic ordering.⁸⁴

CONCLUSIONS

The pervasive influence of local and macroscopic strain associated with phase transitions in the binary system $\text{BiFeO}_3\text{--CaFeO}_{2.5}$ has been investigated indirectly by an analysis of the overall phase relationships and directly for a single representative of the intermediate phase by resonant ultrasound spectroscopy. The general conclusions are as follows. (1) Biquadratic coupling is permitted between multiple order parameters of the system. This is sufficiently strong for coupling between ferroelectric polarization, octahedral tilting, and cation/oxygen/vacancy ordering to determine the stability fields of the $R3c$, $Pnma$, and tetragonal/orthorhombic structures. In particular, coupling between p and q_R appears to be favorable, whereas coupling between q and q_{od} is unfavorable. (2) Linear-quadratic coupling of tilt and ferroelectric order parameters is relatively strong in comparison with coupling of strain with cation/oxygen/vacancy ordering. In marked contrast, linear-quadratic coupling of shear strains with the antiferromagnetic order parameter is weak across the entire solid solution. Elastic stiffening below the Néel point of BCFO 36 confirms that biquadratic ($\lambda e^2 m^2$) terms predominate instead. (3) The crossover from a cycloidal antiferromagnetic ordering scheme to one that is weakly ferromagnetic does not appear to be related to changes in macroscopic strain or to changes in the other macroscopic order parameters. It is proposed, rather, that the key factor would be the development of local strain heterogeneities at low doping levels, which would act to suppress coupling between gradients of the magnetic order parameter. (4) Large dielectric and acoustic loss behavior at low temperatures has highlighted a common loss mechanism involving freezing of oxygen-vacancy motion. The vacancies are mobile via thermal activation, with a wide spectrum of relaxation times under the influence both of electric and stress fields. Similar correlations at high temperatures are attributed to the onset of ionic conductivity and are different in the intermediate phase in comparison with what is seen at low doping.

AUTHOR INFORMATION

Corresponding Author

*E-mail: jas263@cam.ac.uk.

Author Contributions

The manuscript was written with contributions from all authors, and J.S. also carried out the experiments and analyzed the data. All authors have given approval to the final version of the manuscript.

Notes

The authors declare no competing financial interest.

ACKNOWLEDGMENTS

RUS facilities in Cambridge were established through support from the Natural Environment Research Council (NE/

BS05738/1) and from the Engineering and Physical Sciences Research Council (EP/I036079/1) to M.A.C.

REFERENCES

- (1) Catalan, G.; Scott, J. F. *Adv. Mater.* **2009**, *21*, 2463–2485.
- (2) Zhao, T.; Scholl, A.; Zavaliche, F.; Lee, K.; Barry, M.; Doran, A.; Cruz, M. P.; Chu, Y. H.; Ederer, C.; Spaldin, N. A.; Das, R. R.; Kim, D. M.; Baek, S. H.; Eom, C. B.; Ramesh, R. *Nat. Mater.* **2006**, *5*, 823–829.
- (3) Lebeugle, D.; Colson, D.; Forget, A.; Viret, M.; Bataille, A. M.; Gukasov, A. *Phys. Rev. Lett.* **2008**, *100*, 227602-1–227602-4.
- (4) Kothari, D.; Reddy, V. R.; Gupta, A.; Sathe, V.; Banerjee, A.; Gupta, S. M.; Awasthi, A. M. *Appl. Phys. Lett.* **2007**, *91*, 202505-1–202505-3.
- (5) Khomchenko, V. A.; Troyanchuk, I. O.; Többsens, D. M.; Sikolenko, V.; Paixão, J. A. *J. Phys.: Condens. Matter* **2013**, *25*, 135902.
- (6) Chen, S.; Wang, L.; Xuan, H.; Zheng, Y.; Wang, D.; Wu, J.; Du, Y.; Huang, Z. *J. Alloys Compd.* **2010**, *506*, 537–540.
- (7) Chen, W.-t.; Williams, A. J.; Ortega-San-Martin, L.; Li, M.; Sinclair, D. C.; Zhou, W.; Atfield, J. P. *Chem. Mater.* **2009**, *21*, 2085–2093.
- (8) Troyanchuk, I.; Karpinsky, D.; Bushinskii, M.; Prokhnenko, O.; Kopcevicz, M.; Szymczak, R.; Pietosa, J. *J. Exp. Theor. Phys.* **2008**, *107*, 83–89.
- (9) Yang, C.; Liu, C.; Wang, C.; Zhang, W.; Jiang, J. *J. Magn. Magn. Mater.* **2012**, *324*, 1483–1487.
- (10) Ramachandran, B.; Dixit, A.; Naik, R.; Lawes, G.; Rao, M. S. R. *J. Appl. Phys.* **2012**, *111*, 023910-1–023910-5.
- (11) Takeda, Y.; Naka, S.; Takano, M.; Shinjo, T.; Takada, T.; Shimada, M. *Mater. Res. Bull.* **1978**, *13*, 61–66.
- (12) Takeda, T.; Kanno, R.; Kawamoto, Y.; Takano, M.; Kawasaki, S.; Kamiyama, T.; Izumi, F. *Solid State Sci.* **2000**, *2*, 673–687.
- (13) Gibb, T. C.; Herod, A. J.; Munro, D. C.; Peng, N. *J. Mater. Chem.* **1995**, *5*, 1909–1917.
- (14) Woodward, P. M.; Cox, D. E.; Moshopoulou, E.; Sleight, A. W.; Morimoto, S. *Phys. Rev. B* **2000**, *62*, 844–855.
- (15) Kawasaki, S.; Takano, M.; Kanno, R.; Takeda, T.; Fujimori, A. *J. Phys. Soc. Jpn.* **1998**, *67*, 1529–1532.
- (16) Nasu, S.; Abe, T.; Yamamoto, K.; Endo, S.; Takano, M.; Takeda, Y. *Hyperfine Interact.* **1992**, *70*, 1063–1066.
- (17) Lepoittevin, C.; Malo, S.; Barrier, N.; Nguyen, N.; Tendeloo, G. V.; Hervieu, M. *J. Solid State Chem.* **2008**, *181*, 2601–2609.
- (18) Schiemer, J.; Withers, R.; Norén, L.; Liu, Y.; Bourgeois, L.; Stewart, G. *Chem. Mater.* **2009**, *21*, 4223–4232.
- (19) Sardar, K.; Hong, J.; Catalan, G.; Biswas, P. K.; Lees, M. R.; Walton, R. L.; Scott, J. F.; Redfern, S. A. T. *J. Phys.: Condens. Matter* **2012**, *24*, 045905.
- (20) Ross, N. L.; Angel, R.; Seifert, F. *Phys. Earth Planet. Inter.* **2002**, *129*, 145–151.
- (21) Krüger, H.; Kahlenberg, V.; Petricek, V.; Philipp, F.; Werth, W. *J. Solid State Chem.* **2009**, *182*, 1515–1523.
- (22) Takeda, T.; Yamaguchi, Y.; Tomiyoshi, S.; Fukase, M.; Sugimoto, M.; Watanabe, H. *J. Phys. Soc. Jpn.* **1968**, *24*, 446–452.
- (23) Labii, T.; Ceretti, M.; Boubertakh, A.; Paulus, W.; Hamamda, S. *Sci. Technol. A* **2011**, *34*, 29–34.
- (24) Berastegui, P.; Eriksson, S.-G.; Hull, S. *Mater. Res. Bull.* **1999**, *34*, 303–314.
- (25) Krüger, H.; Kahlenberg, V. *Acta Crystallogr., Sect. B* **2005**, *61*, 656–662.
- (26) Redhammer, G. J.; Tippelt, G.; Roth, G.; Amthauer, G. *Am. Mineral.* **2004**, *89*, 405–420.
- (27) Yang, C.-H.; et al. *Nat. Mater.* **2009**, *8*, 485–493.
- (28) Palai, R.; Katiyar, R. S.; Schmid, H.; Tissot, P.; Clark, S. J.; Robertson, J.; Redfern, S. A. T.; Catalan, G.; Scott, J. F. *Phys. Rev. B* **2008**, *77*, 014110-1–014110-11.
- (29) Arnold, D. C.; Knight, K. S.; Morrison, F. D.; Lightfoot, P. *Phys. Rev. Lett.* **2009**, *102*, 027602-1–027602-4.
- (30) Troyanchuk, I.; Karpinsky, D.; Bushinsky, M.; Kovetskaya, M.; Efimova, E.; Eremenko, V. *J. Exp. Theor. Phys.* **2011**, *113*, 1025–1031.
- (31) Arnold, D. C.; Knight, K. S.; Catalan, G.; Redfern, S. A. T.; Scott, J. F.; Lightfoot, P.; Morrison, F. D. *Adv. Funct. Mater.* **2010**, *20*, 2116–2123.
- (32) Li, J.-B.; Rao, G.; Xiao, Y.; Liang, J.; Luo, J.; Liu, G.; Chen, J. *Acta Mater.* **2010**, *58*, 3701–3708.
- (33) Catalan, G.; Sardar, K.; Church, N. S.; Scott, J. F.; Harrison, R. J.; Redfern, S. A. T. *Phys. Rev. B* **2009**, *79*, 212415-1–212415-4.
- (34) Khomchenko, V.; Kiselev, D.; Kopcevicz, M.; Maglione, M.; Shvartsman, V.; Borisov, P.; Kleemann, W.; Lopes, A.; Pogorelov, Y.; Araujo, J.; Rubinger, R.; Sobolev, N.; Vieira, J.; Kholkin, A. *J. Magn. Magn. Mater.* **2009**, *321*, 1692–1698.
- (35) Masó, N.; West, A. R. *Chem. Mater.* **2012**, *24*, 2127–2132.
- (36) Carpenter, M. A.; Salje, E. K. H.; Graeme-Barber, A. *Eur. J. Mineral.* **1998**, *10*, 621–691.
- (37) Ederer, C.; Spaldin, N. A. *Phys. Rev. B* **2005**, *71*, 060401-1–060401-4.
- (38) Sosnowska, I.; Przenioso, R.; Palewicz, A.; Wardecki, D.; Fitch, A. J. *Phys. Soc. Jpn.* **2012**, *81*, 044604-1–044604-4.
- (39) Wang, H.; Yang, C.; Lu, J.; Wu, M.; Su, J.; Li, K.; Zhang, J.; Li, G.; Jin, T.; Kamiyama, T.; Liao, F.; Lin, J.; Wu, Y. *Inorg. Chem.* **2013**, *52*, 2388–2392.
- (40) McKnight, R. E. A.; Howard, C. J.; Carpenter, M. A. *J. Phys.: Condens. Matter* **2009**, *21*, 015901.
- (41) Sosnowska, I.; Neumaier, T. P.; Steichele, E. *J. Phys. C: Solid State Phys.* **1982**, *15*, 4835.
- (42) Przenioso, R.; Regulski, M.; Sosnowska, I. *J. Phys. Soc. Jpn.* **2006**, *75*, 084718-1–084718-3.
- (43) Reetu; Agarwal, A.; Sanghi, S.; Ashima; Ahlawat, N. *J. Appl. Phys.* **2013**, *113*, 023908-1–023908-6.
- (44) Khomchenko, V. A.; Kiselev, D. A.; Vieira, J. M.; Kholkin, A. L.; Sa, M. A.; Pogorelov, Y. G. *Appl. Phys. Lett.* **2007**, *90*, 242901-1–242901-3.
- (45) Khomchenko, V. A.; Kiselev, D. A.; Vieira, J. M.; Jian, L.; Kholkin, A. L.; Lopes, A. M. L.; Pogorelov, Y. G.; Araujo, J. P.; Maglione, M. *J. Appl. Phys.* **2008**, *103*, 024105-1–024105-6.
- (46) Khomchenko, V.; Kiselev, D.; Selezneva, E.; Vieira, J.; Lopes, A.; Pogorelov, Y.; Araujo, J.; Kholkin, A. *Mater. Lett.* **2008**, *62*, 1927–1929.
- (47) Palewicz, A.; Przenioso, R.; Sosnowska, I.; Hewat, A. W. *Acta Crystallogr., Sect. B* **2007**, *63*, 537–544.
- (48) Lee, S.; Fernandez-Diaz, M. T.; Kimura, H.; Noda, Y.; Adroja, D. T.; Lee, S.; Park, J.; Kiryukhin, V.; Cheong, S.-W.; Mostovoy, M.; Park, J.-G. *Phys. Rev. B* **2013**, *88*, 060103-1–060103-5.
- (49) Ederer, C.; Spaldin, N. A. *Phys. Rev. B* **2005**, *71*, 224103-1–224103-9.
- (50) Harrison, R. J.; Redfern, S. A. *Phys. Earth Planet. Inter.* **2002**, *134*, 253–272.
- (51) Harrison, R. J.; Redfern, S. A.; Street, J. *Am. Mineral.* **2003**, *88*, 574–582.
- (52) Harrison, R. J.; Redfern, S. A. T.; Salje, E. K. H. *Phys. Rev. B* **2004**, *69*, 144101-1–144101-10.
- (53) Walsh, J.; Taylor, P.; Buckley, A.; Darling, T.; Schreuer, J.; Carpenter, M. *Phys. Earth Planet. Inter.* **2008**, *167*, 110–117.
- (54) Carpenter, M. A.; Sinogeikin, S. V.; Bass, J. D. *J. Phys.: Condens. Matter* **2010**, *22*, 035404.
- (55) Carpenter, M. A.; Zhang, Z. *Geophys. J. Int.* **2011**, *186*, 279–295.
- (56) Migliori, A.; Sarro, J. L. *Resonant Ultrasound Spectroscopy: Applications to Physics, Materials Measurements, and Nondestructive Evaluation*; Wiley: New York, 1997.
- (57) McKnight, R. E.; Carpenter, M. A.; Darling, T. W.; Buckley, A.; Taylor, P. A. *Am. Mineral.* **2007**, *92*, 1665–1672.
- (58) McKnight, R. E. A.; Moxon, T.; Buckley, A.; Taylor, P. A.; Darling, T. W.; Carpenter, M. A. *J. Phys.: Condens. Matter* **2008**, *20*, 075229.
- (59) Migliori, A.; Maynard, J. D. *Rev. Sci. Instrum.* **2005**, *76*, 121301.
- (60) Ledbetter, H.; Lei, M.; Hermann, A.; Sheng, Z. *Phys. C* **1994**, *225*, 397–403.
- (61) Shang, S. L.; Sheng, G.; Wang, Y.; Chen, L. Q.; Liu, Z. K. *Phys. Rev. B* **2009**, *80*, 052102-1–052102-4.

- (62) Ruello, P.; Pezeril, T.; Avanesyan, S.; Vaudel, G.; Gusev, V.; Infante, I. C.; Dkhil, B. *Appl. Phys. Lett.* **2012**, *100*, 212906-1–212906-3.
- (63) Zhu, J. L.; Feng, S. M.; Wang, L. J.; Jin, C. Q.; Wang, X. H.; Li, L. T.; Li, Y. C.; Li, X. D.; Liu, J. *High Pressure Res.* **2010**, *30*, 265–272.
- (64) Schiemer, J.; Withers, R. L.; Carpenter, M. A.; Liu, Y.; Wang, J. L.; Norén, L.; Li, Q.; Hutchison, W. J. *Phys.: Condens. Matter* **2012**, *24*, 125901.
- (65) Varshni, Y. P. *Phys. Rev. B* **1970**, *2*, 3952–3958.
- (66) Weller, M.; Li, G.; Zhang, J.; Kê, T.; Diehl, J. *Acta Metall.* **1981**, *29*, 1047–1054.
- (67) Schaller, R. J.; Schaller, R.; Fantozzi, G.; Gremaud, G. *Mechanical Spectroscopy Q-1 2001: With Applications to Materials Science*; Trans Tech Publications Limited: Durnten, Switzerland, 2001.
- (68) Carpenter, M. A.; Howard, C. J.; McKnight, R. E. A.; Migliori, A.; Betts, J. B.; Fanelli, V. R. *Phys. Rev. B* **2010**, *82*, 134123-1–134123-16.
- (69) Thomson, R. I.; Jain, P.; Cheetham, A. K.; Carpenter, M. A. *Phys. Rev. B* **2012**, *86*, 214304-1–214304-7.
- (70) Nowick, A. S.; Berry, B. S. *Anelastic Relaxation in Crystalline Solids*; Academic Press: New York, 1972.
- (71) Oravova, L.; Zhang, Z.; Church, N.; Harrison, R. J.; Howard, C. J.; Carpenter, M. A. *J. Phys.: Condens. Matter* **2013**, *25*, 116006.
- (72) Salje, E.; Devarajan, V. *Phase Transitions* **1986**, *6*, 235–247.
- (73) Slonczewski, J. C.; Thomas, H. *Phys. Rev. B* **1970**, *1*, 3599–3608.
- (74) Rehwald, W. *Adv. Phys.* **1973**, *22*, 721–755.
- (75) Carpenter, M. A.; Salje, E. K. H. *Eur. J. Mineral.* **1998**, *10*, 693–812.
- (76) Carpenter, M. A.; McKnight, R. E. A.; Howard, C. J.; Zhou, Q.; Kennedy, B. J.; Knight, K. S. *Phys. Rev. B* **2009**, *80*, 214101-1–214101-8.
- (77) Boffa Ballaran, T.; Carpenter, M. A.; Domeneghetti, M. C.; Salje, E. K. H.; Tazzoli, V. *Am. Mineral.* **1998**, *83*, 434–443.
- (78) Boffa Ballaran, T.; Carpenter, M. A.; Geiger, C. A.; Koziol, A. M. *Phys. Chem. Miner.* **1999**, *26*, 554–569.
- (79) Atkinson, A. J.; Carpenter, M. A.; Salje, E. K. H. *Eur. J. Mineral.* **1999**, *11*, 7–21.
- (80) Salje, E. K.; Carpenter, M. A.; Malcherek, T.; Boffa Ballaran, T. *Eur. J. Mineral.* **2000**, *12*, 503–519.
- (81) Carpenter, M. A.; Ballaran, B. *EMU Notes Mineral.* **2001**, *3*, 155.
- (82) Tarantino, S. C.; Boffa Ballaran, T.; Carpenter, M. A.; Domeneghetti, M. C.; Tazzoli, V. *Eur. J. Mineral.* **2002**, *14*, 537–547.
- (83) Boffa Ballaran, T.; Carpenter, M. A.; Ross, N. L. *Mineral. Mag.* **2001**, *65*, 339–350.
- (84) Tirupathi, P.; Chandra, A. *J. Alloys Compd.* **2013**, *564*, 151–157.